

# WIDGET: System Performance and GRB Prompt Optical Observations

Yuji URATA<sup>1</sup>, Makoto S. TASHIRO<sup>2</sup>, Toru TAMAGAWA<sup>3,4</sup>, Fumihiko USUI<sup>5</sup>,  
Makoto KUWAHARA<sup>3,4</sup>, Hungmiao LIN<sup>1</sup>, Shoichi KAGEYAMA<sup>3,4</sup>, Wataru IWAKIRI<sup>2</sup>,  
Takako SUGASAHARA<sup>2</sup>, Kazuki TAKAHARA<sup>2</sup>, Natsuki KODAKA<sup>2</sup>,  
Keiichi ABE<sup>2</sup>, Keisuke MASUNO<sup>2</sup>, and Kaori ONDA<sup>2</sup>

<sup>1</sup>*Institute of Astronomy, National Central University, Chung-Li 32054, Taiwan*

*urata@astro.ncu.edu.tw*

<sup>2</sup>*Department of Physics, Saitama University, Shimo-Okubo 255, Sakura, Saitama 338-8570*

<sup>3</sup>*RIKEN (Institute of Physical and Chemical Research), 2-1 Hirosawa, Wako, Saitama 351-0198*

<sup>4</sup>*Tokyo University of Science, 1-3 Kagurazaka, Shinjyuku, Tokyo*

<sup>5</sup>*Japan Aerospace Exploration Agency, Institute of Space and Astronautical Science*

*3-1-1 Yoshinodai, Chuo-ku, Sagamihara, Kanagawa 252-5210*

(Received 2010 July 5; accepted 2010 October 21)

## Abstract

The WIDeField telescope for Gamma-ray burst Early Timing (WIDGET) is used for a fully automated, ultra-wide-field survey aimed at detecting the prompt optical emission associated with Gamma-ray Bursts (GRBs). WIDGET surveys the *HETE-2* and *Swift*/BAT pointing directions covering a total field of view of  $62^\circ \times 62^\circ$  every 10 seconds using an unfiltered system. This monitoring survey allows exploration of the optical emission before the  $\gamma$ -ray trigger. The unfiltered magnitude is well converted to the SDSS  $r'$  system at a 0.1 mag level. Since 2004, WIDGET has made a total of ten simultaneous and one pre-trigger GRB observations. The efficiency of synchronized observation with *HETE-2* is four times better than that of *Swift*. There has been no bright optical emission similar to that from GRB 080319B. The statistical analysis implies that GRB080319B is a rare event. This paper summarizes the design and operation of the WIDGET system and the simultaneous GRB observations obtained with this instrument.

**Key words:** Gamma-Ray Burst:Optical emission

## 1. Introduction

The prompt emission of Gamma-ray Bursts (GRBs) has become an intriguing topic in modern astrophysics. In particular, the optical flash associated with  $\gamma$ -ray emission poses significant challenges both observational and theoretical. In 1999, the robotic instrument *ROTSE* successfully detected the first optical flash from GRB990123 with a brightness that reached 8.9 mag 50 s after the burst (Akerlof et al. 1999). Recently, the optical flash associated with GRB080319B has been detected at high signal to noise using a number of small telescopes (Racusin et al. 2008; Woźniak et al. 2009; Bloom et al. 2009), and could have been observed without any instruments. These are bright enough to be detected by small aperture instruments. Surprisingly, the bright optical emission of GRB 080319B was also detected by the simple weather monitoring equipment at Mt. Lemmon Observatory operated by KASI in Korea (Urata et al., 2010 in prep). In addition to these two events, small robotic telescopes have also made prompt optical observations during  $\gamma$ -ray activity such as of GRB041219A (Vestrand et al. 2006), GRB050820A (Vestrand et al. 2005), GRB051111 (Yost et al. 2007) and GRB061121 (Page et al. 2007). Even though there were only six optical detections before the  $\gamma$ -ray radiation died off, three major emission models have been used to explain these optical emissions: (1) reverse shock (e.g. Kobayashi (2000); Kobayashi & Sari (2000)); (2) synchrotron self Compton (e.g. Racusin et al. (2008)); and (3) simple synchrotron radiation from the standard internal shock (e.g. Shen & Zhang (2009)). Furthermore, Yamazaki (2009) predicts a possible optical precursor before the rise of the  $\gamma$ -ray emission which would explain the plateau phase in the X-ray afterglows.

The number of robotic telescopes responding to GRB detection alerts through the GRB Coordinate Network (GCN) increased starting from the *HETE-2* era. These telescopes however are not sufficient to make simultaneous and pre-trigger observations with prompt  $\gamma$ -ray emission. Since they respond to the GRB position alert from satellites, the delay time is always longer than several tens of seconds. Therefore, a  $\gamma$ -ray/X-ray precursor or longer duration event is required to make optical observations simultaneous with  $\gamma$ -rays. In order to break through this limitation, we have constructed and began operating the WIDeField telescope for Gamma-ray Burst Early Timing (WIDGET) since 2005 (Tamagawa et al. 2005). There are three other similar instruments worldwide, the so-called “Pi of the Sky” (Sokolowski et al. 2009), RAPTOR (Woźniak et al. 2009) and TORTORA (Greco et al. 2009). These three cover the sky in the Western hemisphere. Only WIDGET covers the Eastern hemisphere. In this paper, we report on the development, performance and the first results of WIDGET.

## 2. The *WIDGET* System

### 2.1. Overview

*WIDGET* is a fully robotic telescope system placed at the Kiso astronomical observatory of the Institute of Astronomy, Faculty of Science, University of Tokyo. The main aim of this system is to monitor the *Swift* field-of-view and to detect GRB optical flashes or possible optical precursors. The prototype systems (called *WIDGET1* and *WIDGET1.5*) was operated at the Akeno observatory of the Institute for Cosmic Ray Research University of Tokyo, which was used for the Akeno Giant Air Shower Array (AGASA; Hayashida et al. 1996). During the two year operation in Akeno, a fully robotic system was established, and the system performance and site condition of Akeno were evaluated (Tamagawa et al. 2005). System updates are summarized in table 1. Through these studies, we found that a dark sky and a new improved optical system are required for more efficient monitoring. We had moved the system to the Kiso astronomical observatory in 2006 November. This was done to improve the sky background level and weather conditions. In addition, this allows us to connect the *WIDGET* observations with monitoring of afterglows by the 105cm Schmidt telescope at the same site without weather risk. The telescope has been observing afterglows (e.g. Urata et al. 2003; Urata et al. 2004; Huang et al. 2005; Urata et al. 2007a; Urata et al. 2007c; Huang et al. 2007). In November 2006 we began the installation of a new observatory hut and weather monitoring system and performed testing. After three months of refining, full operation started in February, 2007.

The current *WIDGET* system (hereafter *WIDGET2*) consists of four optics systems, an automated observatory hut equipped with a cluster of control computers and a house keeping system for unattended service. *WIDGET2* is powered by the commercial 100-volt alternating current source and the commands and data are transmitted via the digital service line (DSL).

The telescope, with its related computers and electronics are housed in the observatory hut with its one-direction sliding roof. Figure 1 shows a schematic of the control system of cameras, the monitoring system, the polar mount, and remaining equipment. The entire system is controlled by five computers and a relay board box inside the observatory hut.

The time reference signal is provided by a network timing protocol (NTP) server and a radio clock with an average error of less than 1 s. The power supply for equipment such as CCD cameras, polar mounts, control PCs can be turned off/on remotely via relay boards.

### 2.2. Observational Hut

The observatory hut is custom built by Human Comm Co. Ltd.. Its dimensions are  $H \times W \times L = 2 \times 2 \times 3$  meters. As shown in Figure 2, the sliding roof on the optics side the sliding roof dives down when in observation mode so as not to interfere with the field of view of optics down to an altitude of  $20^\circ$ . The power line is connected and controlled by the relay boards, which accept commands from a control PC via a socket connection. The roof is nominally

opened and closed by preplanned commands, although if the weather station detects rainfall the roof can be closed by the automatically generated command. Two small air ventilator fans made for sailboat usage are installed on top of the roof. The power is supplied by the system's own solar battery. The temperature beneath the roof remains nominal even on sunny summer days.

### 2.3. Weather stations

The weather sensing equipment placed outside and inside the hut monitors rainfall, air temperature, wind speed and humidity. The opening and closing of the sliding roof at night is fully dependent on rain detection by the rain sensor. There are a total of eight rain sensor sets mounted around the roof to enable detection of rain regardless of the direction it come from. The inclination of the rain sensors could have some dependence on the direction. For the preservation of the instruments inside the observing hut, the roof closes immediately when any of the sensors detects rain fall. To avoid the chattering that occurs under misty conditions or light rainfall that could lead to frequent opening and closing of the roof, we set the hardware time delay to 30 minutes after the changing of the rain status (rain to fine).

### 2.4. Optics

The optics system consists of four sets of commercial CCD camera and lens sets. We employ Apogee Alta U10 CCD camera carrying a  $2048 \times 2048$  format Atmel THX7899 CCD chip of 14-micron pixels. The CCD chip is the front-illuminated type with a quantum efficiency of 38 % for 720 nm optical light. As shown in figure 3, the camera body is compact ( $15 \times 15 \times 6.35$  cm) and light (1.4 kg) enough to allow the installation of an array of four cameras on a single small polar mount. Each camera is equipped with a 50 mm f/1.2 Canon EF lens. Each lens has a special lens baffle to block other light sources from the ground and to prevent water condensations during observing runs. A continuous flow of dry air is also provided to the surface of the lens to avoid water condensations. This configuration yields a  $32^\circ \times 32^\circ$  field of view for each segment. As shown in Figure 4, the total field of view with  $2^\circ$  field overlap between each segment is  $62^\circ \times 62^\circ$  which covers about 33% of the *Swift*/BAT observing field. The electronics on-board the CCD camera have been optimized to provide fast readout of the entire array within 5 s with a 16 bit AD converter through an USB2.0 line. The standard exposure during operation is 5 s, so that we obtain sky images every 10 s including the readout time. This exposure cycle provides an optimal balance between sensitivity and time-resolution.

There is a thermoelectric cooler with forced air control for the CCD cooling. Since the cooler delivers a maximum temperature difference of  $45^\circ\text{C}$  below the ambient temperature, the actual temperature depends on the season. The minimum and maximum are  $-40^\circ\text{C}$  in winter and  $-15^\circ\text{C}$  in summer. Bias and dark analysis confirms the read out noise and dark level are  $14.7e^-$  and  $1.1 e^- \text{ pixel}^{-1} \text{ s}^{-1}$  at  $-15^\circ\text{C}$ , respectively. Hence, the read out noise is about three times larger than the dark level with the daily standard exposure time.

## 2.5. Polar-mount

As shown in figure 2, the optics is attached to a Takahashi NJP Temma-2 polar mount. The polar mount is controlled via a serial line by a PC running Linux OS with custom control software. The maximum slewing speed is  $90 \text{ arcmin s}^{-1}$ , which is sufficient to make effective monitoring observations for the *Swift*'s monitoring fields. Due to the shape of the mount with the camera array, there are some areas where the optics hit the pillar of the mount. Manual inspection shows just where these areas are. Although these areas do not affect normal operation, with imposed software operational limits.

## 3. Daily operation and observations

The daily operation is fully managed by automated observing scripts. Each script controls the observation huts, mount, cameras and weather monitoring system individually. To store observational data in order, the CCD operation script gathers pointing information and coordinates, and records them in the fits header unit. Daily operating status, including weather station status can be checked via the internal web site which is updated every 5 minutes. The stored data is summarized and transmitted via the Internet with house keeping data and operation reports every morning. Email notification is sent to a human operator in case of problems related to the observation huts. The duty scientist checks the system and observation status once a day. The telescope automatically observes the sky every night that is not rainy. Thirty dark frames are obtained before and after monitoring observations. Such automatic observations offer maximum monitoring efficiency for observations prior to and simultaneous with the GRB observation even under partially cloudy condition. The observation field is selected based on the “*Swift* Pointing Dir” alert from the GRB Coordinate Network (GCN). When the *Swift* pointing direction is not observable, such as for southern sky targets ( $\text{Dec} > -30^\circ$ ) or due to objects obstructing the horizon at the Kiso observatory, WIDGET observes the zenith direction without sidereal tracking. These images are stacked using median filtering to obtain sky flat frames. The previous systems (WIDGET1.0 and 1.5) observed mainly the *HETE-2* field of view and the zenith. WIDGET2 is monitoring these fields by repeated unfiltered 5 s exposures.

The WIDGET2 system has no-quick response mode like the robotic follow-up system, such as *ROTSE* or *RAPTOR*. Once a GRB occurs, WIDGET observes the field, until receiving the next *Swift* pointing information or until morning. When *Swift* detects a new GRB, the duty scientist is notified by cellphone. The duty scientist checks the weather condition at the Kiso Observatory as well as the overlap between the WIDGET2 FOV and the GRB's position using a special script. Since WIDGET covers 33% of the *Swift*/BAT FOV., some of events are out of its FOV. If the GRB is in the FOV, the data sets for the GRB field before and around the GRB trigger time are manually transferred from the Kiso Observatory to RIKEN and Saitama University via the Internet. As summarized in table 3, all three WIDGET systems

(WIDGET 1.0, 1.5 and 2.0) have hunted 11 GRB fields before their trigger event, except in unfavorable weather conditions. The time coverage of pre-trigger monitoring is fully dependent on the satellite observing strategy. In case of *HETE-2* (anit-solar pointing), WIDGET was able to obtain long monitoring data such as for GRB050408 (de Ugarte Postigo et al. 2007), GRB051028 (Urata et al. 2007b) and GRB060121A. In the *Swift* era, the time coverage is shorter (typically several ten minutes) due to *Swift*'s short pointings.

#### 4. Calibration and System Performance

System evaluation is performed using daily data sets. The main concerns are astrometric and photometric calibration to enable prompt optical monitoring of GRBs. Since joint observation and analysis with larger aperture follow-up telescopes (e.g., the Kiso Schmidt telescope; the Lulin One meter telescopes) are also one of the key issues for GRB sciences, the magnitude conversion to standard photometric filters is critical. Another crucial application is as a new transient surveyor which can search for highly variable optical transients (e.g. OT J004240.69+405142.0 (de la Fuente Marcos et al. 2009)) utilizing entire WIDGET2 images. For effective analysis of the huge amounts of data, the process of astrometric pipeline reduction is essential.

A standard preprocessing routine based on IRAF is employed, including bias/dark subtraction, and flat-fielding corrections with appropriate calibration data.

##### 4.1. Astrometric Calibration

Astrometric calibration is made using daily observational data. The main goal is to identify GRB positions with less than 1 pixel position accuracy. The typical position accuracies are  $2 \sim 3''$  for X-ray (*Swift*/XRT) and less than  $1''$  for optical data, respectively. This position accuracy requires astrometric accuracy of less than 1 pixel size of WIDGET for identification of the GRB position. This effort is also critical to reduce contamination from other sources.

The geometric distortion effect from the lens optics is well described by a polynomial function (Guan et al. 1997; Hata et al. 2002). According to the generic features, the effect can be ignored at the center of the images, but becomes more significant with the distance from the optical axis. In order to check the effect on the astrometry of the WIDGET2 images, we performed astrometry using the central one-ninth part of the image expected to be affected by the non-geometric. For the astrometric standard, we employ the Tycho2.0 catalog, which is particularly suited to use for astrometric use in the point of sky coverage with bright enough stars ( $V_T < 11.5$ ) for WIDGET and for position accuracy ( $\pm 0.6$  mas). We selected 21 non-saturated stars brighter than  $V_T < 9$  mag in the field-of-view then identify their coordinates from the Tycho2.0 catalog. The X-Y positions of each star in the frame are measured using the IRAF `center` command. Using `ccmap` of IRAF task, we calculate the translation form with a tangent sky geometry projection. From this fitting, we obtain the pixel scale and field

of view are  $55''$  and  $10.^{\circ}7 \times 10.^{\circ}7$ , respectively. The spatial resolution and the field-of-view are consistent with the expected values from the optics and CCD combination, respectively. In addition, the position accuracy satisfies our scientific requirement.

We evaluated the differences between actual positions of catalogued stars on the images and expected coordinates calculated using the translation function. Figure 5 shows the differences along the interval from the optical axis. A geometrical model of field distortion using a 4th-order polynomial function is employed to describe this,

$$r - r_{tan} = ar + br^2 + cr^3 + dr^4, \quad (1)$$

where  $r$  and  $r_{tan}$  are distances from the optical axis in units of pixels for catalog star positions on the CCD images and expected position as obtained by the translation function. As shown in figure 5, the difference can be well fitted according to equation 1. This result is consistent with those employing other strategies for a simple lens system (e.g. Guan et al. (1997); Hata et al. (2002)).

We then correct the distortion using the IRAF `GEOMAP` and `GEOTRAN` tasks and perform astrometry over the full image area in the same manner as described above. The astrometric accuracy is much improved with  $45''$  rms deviation, similar to the value for the central region.

#### 4.2. Photometric Calibration

On the CCD chip the U10 as peak QE curve is at 720 nm which is similar to the band-bass of Johnson-Cosinus  $Rc$ -band and SDSS  $r'/i'$  filters. It is expected that the best strategy for photometric calibration is to make a comparison with the  $Rc$ -band or  $r'/i'$ -band brightness. This is also same assumption with the unfiltered telescope system Henden (2000). In addition, this conversion to  $Rc$  or  $r'$  bands allows us to connect with further afterglow observations. As a first step, we check the variance from the Hipparcos  $B_T$  and  $V_T$  band catalog magnitudes recorded in the Tycho-2.0 catalog using daily data sets. Since Tycho-2.0 covers the whole sky and contains bright stars ( $m < 9$  mag), it is easy to find many stars on the WIDGET images. Even using  $V_T$  band, the scatter is about  $0.2 \sim 0.3$  in magnitude. This is because combination effect of the color dependence of the CCD response and various spectrum of photometric comparison stars. Since the spectrum of the prompt optical emission is totally unknown, this calibration method could have a large systematic error.

For better calibrations, we employ two photometric catalogs; (1) Landolt standard stars; and (2) Guide star photometric catalog II. The tentative limiting magnitude of the current system derived from the Tycho2.0  $V_T$ -band is deep enough to make a comparison with these two catalogues, including the redder bands. These two photometric catalogs are appropriate for WIDGET data calibration. The Landolt catalogue has been used for current optical observations even for 8-m class telescopes. The GSPC-II catalog was created to provide photometric calibrators for the HST Guide Star Catalog. These stars are randomly distributed throughout the whole sky with huge volume being 9 mag in the  $Rc$ -band. In order to perform additional

photometric calibration, we obtain images centered on the Landolt standard star field (SA95). This is in addition to normal daily observations with 5, 60, 120 and 180 s exposures made under remote operation from the RIKEN site on 4th November 2007. The WIDGET field of view is wide enough to image the entire SA95 field together with the bright spectroscopic standard star HR1544. Five Landolt’s standard stars (95-15, 95-43, 95-74, 95-96 and 95-149) can be detected in the images with 5 s exposures. The faintest one is 95-74 ( $R = 10.93$ ). The color range of  $(B - V)$  is from 0.1 to 1.89, which covers the typical colors of optical afterglow. These stars are located at similar airmass 1.12 for HR1544 and 1.27 for the SA95 field, respectively. We also selected GSPC stars at the same airmass (1.15) with HR 1544. Therefore, the expected differences of atmospheric extinction for these stars are 0.01 mag level which is not significant for this calibration.

Based on the standard aperture photometry, we measure the instrumental magnitude of WIDGET. Figure 6 shows a comparison of the B, V, Rc and Ic magnitudes for the Landolt catalog. The fits made using a simple liner function yield an rms of 0.50 (B), 0.20 (V), 0.07 (Rc) and 0.16 (Ic), respectively. Hence, the WIDGET magnitude is well matched to standard Rc magnitude. We also add GSPCII stars to improve the statistics and to cover bright end of the magnitude distribution. As can be seen in figure 7 the fitting remains consistent with the simple conversion to the Rc-band magnitude within the 0.1 mag scatter. The typical limiting magnitudes in the Rc-band for each exposure are 11.3 (5 s), 12.9 (60 s), 12.8 (120 s) and 12.9 (180 s), respectively.

We also make a comparison with the SDSS system using the modified Tycho-2.0 catalog, as described by Ofek (2008). This is needed because the number density of bright ( $< 12$  mag) Landolt and GSPCII stars is insufficient to perform photometric calibration for numerous GRB fields. Typically, there are no Landolt and only a few GSPCII stars located near the GRB fields. (Ofek 2008) constructed an all-sky catalog of griz magnitudes of bright stars ( $V < 12$ ) based on the Tycho-2.0 catalog, which makes it easy to find a larger number of bright stars around GRB positions on WIDGET images. This helps to minimize the photometric systematic error due to the spatial differences between references and GRB positions. Figure 8 shows the results obtained in the same manner with Landolt and GSPSII calibrations. The rms scatter of transformation between catalog magnitude and instrumental magnitude is 0.59 mag at  $g'$ , 0.17 mag at  $r'$ , 0.19 mag at  $i'$  and 0.32 mag at  $z'$ , respectively. It can be seen that the instrumental magnitudes are sufficiently well reproduced for  $r'$  and  $i'$  bands. We also formulate an equation for transformation from the instrumental magnitude to the  $r'$ -band system utilizing color information:  $r' = m_{inst} - 8.15 + 0.17 \times (g' - i')$ . Here,  $m_{inst}$  indicates the instrumental magnitudes derived with the pseudo zero-magnitude as 25.00 mag. Figure 9 shows a comparison of the instrumental magnitudes transformed onto the standard system. The scatter becomes 0.12 mag which is 0.05 mag better than the initial result.



## 5. Simultaneous optical and $\gamma$ -ray observations of GRBs

We collected a total of ten simultaneous GRB observations, including one short GRB and one pre-trigger observations, for GRB060121A. Three of those bursts were localized by *HETE-2*, and the remaining eight are *Swift* events. Table 3 shows a summary of the fluence of the  $\gamma$ -ray emission, duration, redshift and afterglow brightness. Unfortunately, there is no GRB with an optical afterglow as bright as GRB030329 or GRB080319B. These fluences of those bursts are also an order of magnitude below that of GRB080319B. Since WIDGET is the only instrument covering the Asian region, there are no coincident observations from similar instruments such as with “Pi of the Sky (Las Capanas)”, TORTORA (La Silla) or RAPTOR (Fenton Hill, US) which cover the Western hemisphere. Therefore, we missed the extremely bright optical emission associated with GRB080319B because it occurred in the afternoon in Japan. Compared with the latter three instruments, WIDGET has the widest field of view, as summarized in table 2. This means that the number of simultaneous observations by WIDGET is about twice that of similar instruments such as “Pi of the Sky” (Sokolowski et al. 2009). There are also seven *HETE-2* events that occurred under cloudy conditions. When we include cloudy events, the simultaneous observational ratio for the *HETE-2* events is 6.7 GRBs/yr, which is consistent with the expected ratio and four times higher than that of *Swift*. One of the main reasons for the significant differences between the *HETE-2* and *Swift* ratios is the pointing strategy. *HETE-2* monitored the anti-solar direction, while the distribution of *Swift* pointings is mostly uniform. Anti-solar monitoring is easier to achieve for ground-based telescopes. The next generation GRB satellite SVOM will explore the anti-Sun direction and is expected to localize about 70 GRB per year (Schanne et al. 2010). WIDGET will be able to make 3~4 observations per year by monitoring the SVOM FOV.

All 11 GRB positions in table 3 were covered by WIDGET before the onset of the  $\gamma$ -ray emissions. In order to search for optical precursors, we checked all available data sets for the presence of emission at the alerted position evaluating CCD ADU counts, sky background, and statistical error for time series. The GRB region is selected using a 2 pixel aperture centered on the afterglow position. In the GRB050408 case, there was a significant emission besides cosmic-ray events 4.7 hrs before the trigger. However, the object was moving just passing through the GRB position. Except for this moving object, there was no significant optical emission. Besides GRB050408, there are no other significant detections at the other ten GRB positions. Note that the X-ray afterglows of four events (GRB051227, GRB060211A, GRB060413 and GRB071021) show a clear plateau phase. According to Yamazaki (2009), there is a possible optical precursor  $10^3 - 10^4$  s before the trigger. We did not detect any significant emission from these events in the time region summarized in table 3.

We also constructed a broadband SED that includes  $\gamma$ -ray and X-ray data from *HETE-2*, *Swift* and *Suzaku*/WAM. Since GRB060413 has high galactic extinction ( $A_V=6.3$ ), it is excluded

from this joint analysis. Analysis shows that there is no bright optical emission similar to that from GRB080319B ( $V \sim 6$  mag.). This implies that events like GRB 080319B as the extreme prompt behavior is understood by synchrotron self-Compton are statistically rare. Figures 10 and 11 show the time resolved SEDs for GRB050408 and GRB060323, respectively. These SEDs show that the WIDGET limits are below or marginally consistent with extrapolations from the low-energy power law of the prompt  $\gamma$ -ray spectrum. The absence of the optical emission can be explained assuming that the prompt  $\gamma$ -ray and X-ray emissions are the same synchrotron radiation with the synchrotron self-absorption between X-ray and optical bands ( $\nu_m < \nu_{opt} < \nu_a$  or  $\nu_{opt} < \nu_a < \nu_m$  case). Here,  $\nu_m$ ,  $\nu_{opt}$  and  $\nu_a$  are the frequencies of the observed characteristic emission, optical band and self-absorption, respectively. Another possibility is the  $\nu_a < \nu_{opt} < \nu_m$  case (for details see Shen & Zhang (2009)).

## 6. Conclusions

We summarize the system development, operation, as well as GRB observations.

- Fully robotic instruments for observation of prompt optical emission associated with GRB were constructed. The first system monitored the *HETE-2* field of view between 2004 and 2007. The current system is making simultaneous monitoring for *Swift*/BAT with 5-second exposures.
- The geometric distortion of the optical system is evaluated, and astrometric calibration against with the Tycho-2.0 catalog is performed. The distortion is well described with a 4th order polynomial function. After the distortion correction, the astrometric accuracy is less than 1 pixel level.
- Photometric calibration against with the Landolt photometric catalog and modified Tycho-2.0 catalog is performed. WIDGET's unfiltered magnitude is well converted to the SDSS  $r'$  system at a 10% level.
- WIDGET made 11 GRB observations preceding the  $\gamma$ -ray trigger. The efficiency of the synchronized observations with *HETE-2* is four times better than that of *Swift*. The time resolved SEDs for two GRBs (GRB050408 and GRB060323) show that the WIDGET limits are below or marginally consistent with the extrapolations of the  $\gamma$ -ray spectrum. The absence of the optical emission can be explained assuming that the prompt  $\gamma$ -ray and X-ray emissions are the same synchrotron radiation with the self-absorption between X-ray and optical bands.

We thank the staff at the Kiso Observatory for the various arrangements. The project is supported by the RIKEN director's fund in FY2003 and FY2004 (PI TT) and a Grant-in-Aid from the Ministry of Education, Culture, Sports, Science and Technology of Japan (1834005; PI: MST, 18001842; YU). This work is partly supported by grants NSC 98-2112-M-008-003-MY3 (YU).

## References

- Akerlof, C., et al. 1999, *Nature*, 398, 400
- Bloom, J., et al. 2009, *ApJ*, 691, 723
- de la Fuente Marcos, R., et al. 2009 *New Astronomy* 14, 214
- de Ugarte Postigo, A., et al. 2007, *A&A*, 462, L57
- Greco, G., et al. 2009, *Mem. S.A.It. Vol 80*, 231
- Guan, H., Aoki, S., & Ejiri, K., 1997, *Richoh Technical Report No23*. 48
- Hata, K., Maruyama, M., & Toriihara, M., *Oobayashi gumi technical report 2002*, No. 65, 71
- Hayashida, N., et al. 1996, *Physical Review Letters*, 77, 1000
- Henden, A. A., 2000, *Journal AAVSO vol. 29*, page 35.
- Huang, K. Y., et al. 2005, *ApJL*, 628, L93
- Huang, K. Y., et al. 2007, *ApJL*, 654, L25
- Kobayashi, S. 2000, *ApJ*, 545, 807
- Kobayashi, S., & Sari, R. 2000, *ApJ*, 542, 819
- Ofek, E. O, 2008, *PASP*, 120, 1128
- Page, K. L., et al. 2007, *ApJ*, 663, 1125
- Racusin, J. L., et al. 2008, *Nature*, 455, 183
- Schanne, S., et al. 2010, *arXiv:1005.5008*
- Shen, R.-F., & Zhang, B. 2009, *MNRAS*, 398, 1936
- Sokolowski, M., et al. 2009, *American Institute of Physics Conference Series*, 1133, 306
- Tamagawa, T. et al. 2005, *NCimC*, 28, 771
- Urata, Y., et al. 2007, *ApJL*, 668, L95
- Urata Y., et al. 2007, *PASJ*, 59L, 29
- Urata, Y., et al. 2007, *ApJL*, 655, L81
- Urata Y. et al 2005, *NCimC*, 28, 775
- Urata, Y., et al. 2004, *ApJL*, 601, L17
- Urata, Y., et al. 2003, *ApJL*, 595, L21
- Vestrand, W. T., et al. 2006, *Nature*, 442, 172
- Vestrand, W. T., et al. 2005, *Nature*, 435, 178
- Wozniak P.R., et al. 2009, *ApJ*, 691 495
- Yamazaki, R. 2009, *ApJL*, 690, L118
- Yost, S. A., et al. 2007, *ApJ*, 657, 925

**Table 1.** WIDGET systems

Version	FOV.	Lens	Pixel size	Site	Operation period
WIDGET1.0	$(62^\circ \times 62^\circ) \times 1$	Cannon EF 24mm f/1.4	$1'.82 \times 1'.82$	Akeno	2004.07–2005.11
WIDGET1.5	$(42^\circ \times 42^\circ) \times 3$	Cannon EF 35mm f/1.4	$1'.23 \times 1'.23$	Akeno	2005.11–2006.11
WIDGET2.0	$(32^\circ \times 32^\circ) \times 4$	Cannon EF 50mm f/1.2	$0'.94 \times 0'.94$	Kiso	2007.02–current

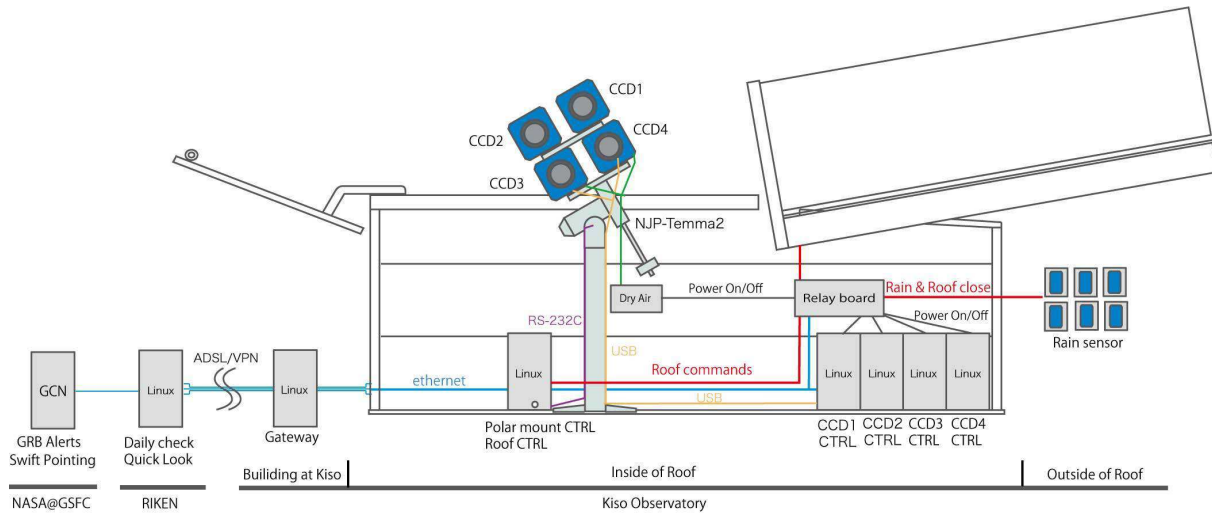


**Fig. 1.** Hardware block diagram of WIDGET.



**Fig. 2.** The observing huts of WIDGET.



**Fig. 3.** The WIDGET optics attached to a polar mount.

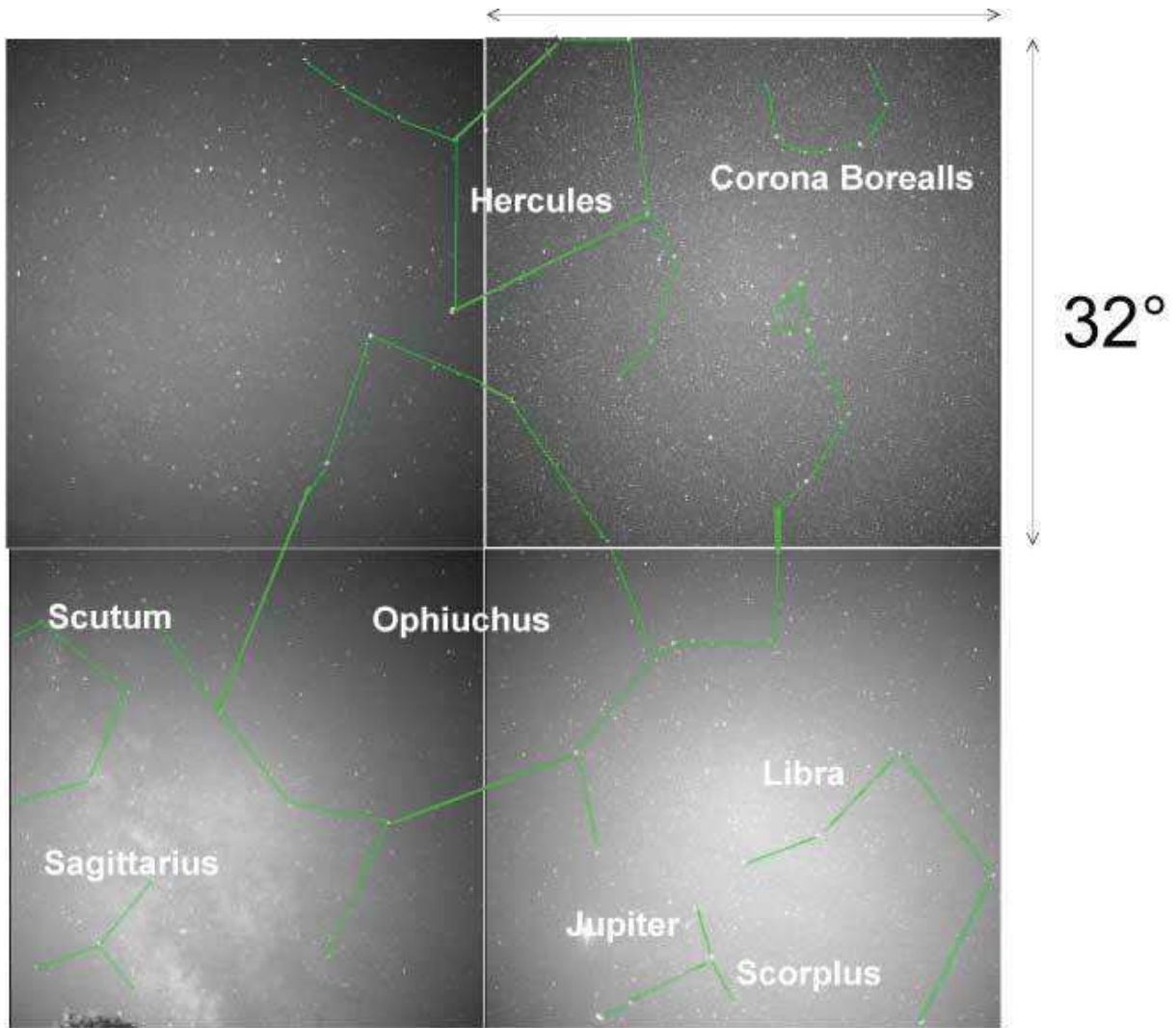


**Fig. 4.** The entire field of view of the WIDGET-2.

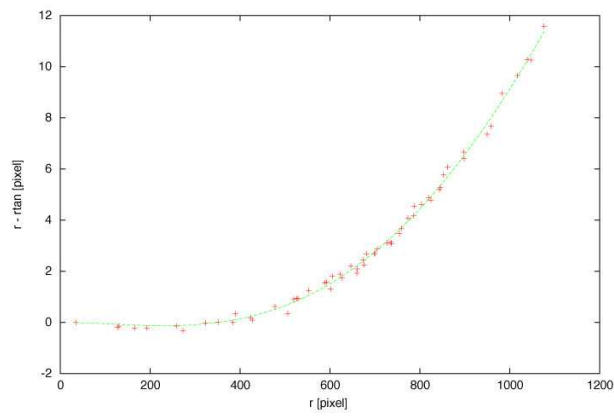


**Fig. 5.** Optical geometric distortion of the WIDGET lens. The dashed line shows the geometrical solution (see text).

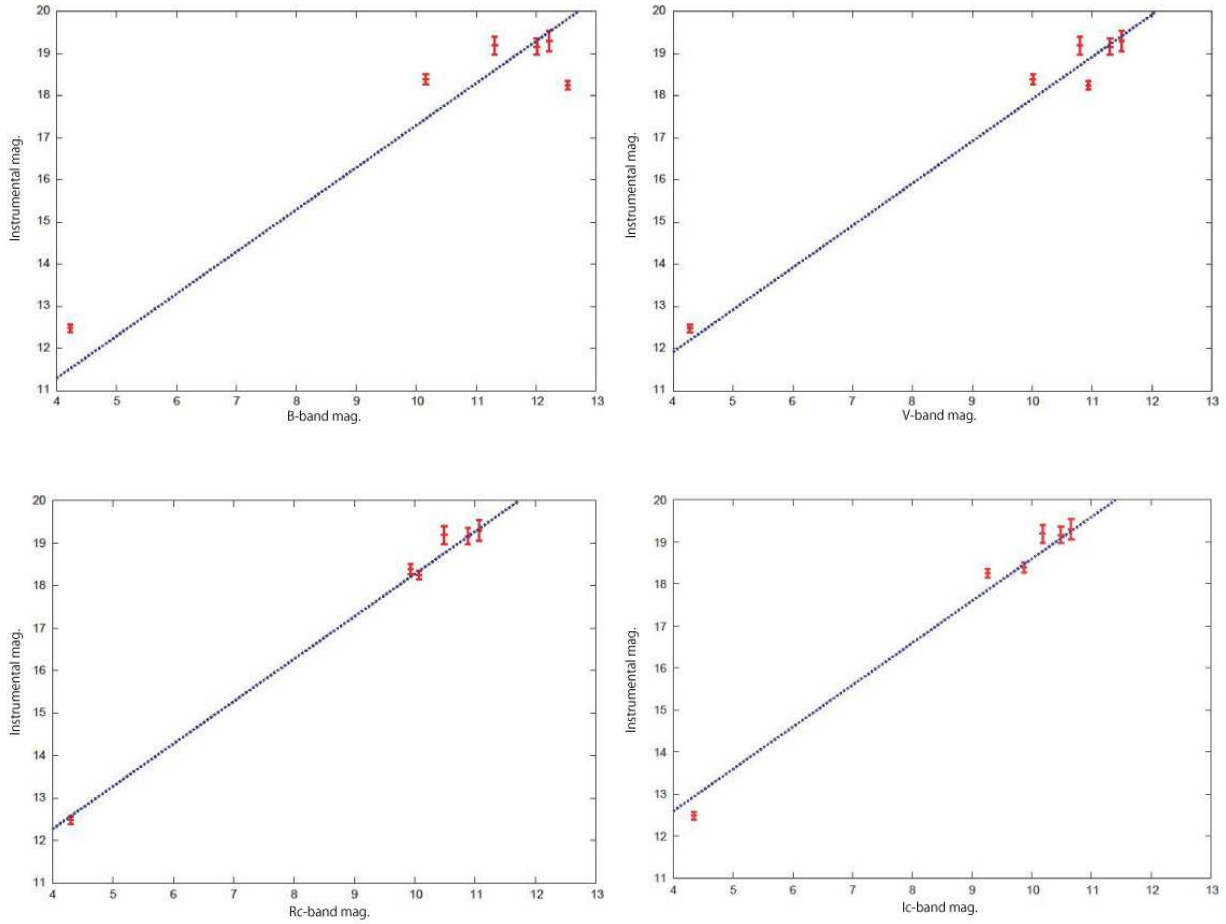


**Fig. 6.** The photometric comparison of the WIDGET instrumental magnitude with B, V, Rc, Ic magnitudes of the Landolt stars and the spectroscopic standard star HR1544.

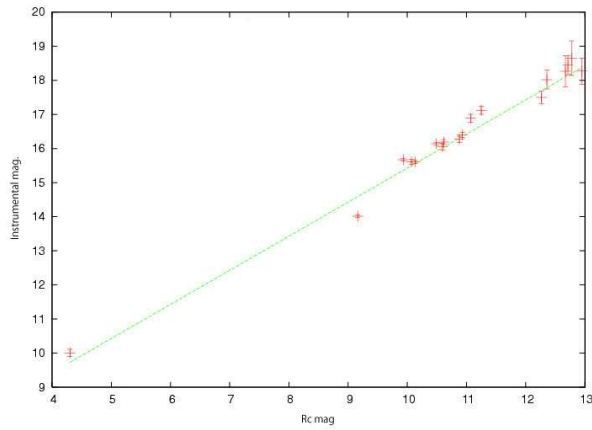


**Fig. 7.** The R-band comparison of the WIDGET instrumental magnitudes against with the Landolt SA95 field, HR1544 and GSPC catalog.

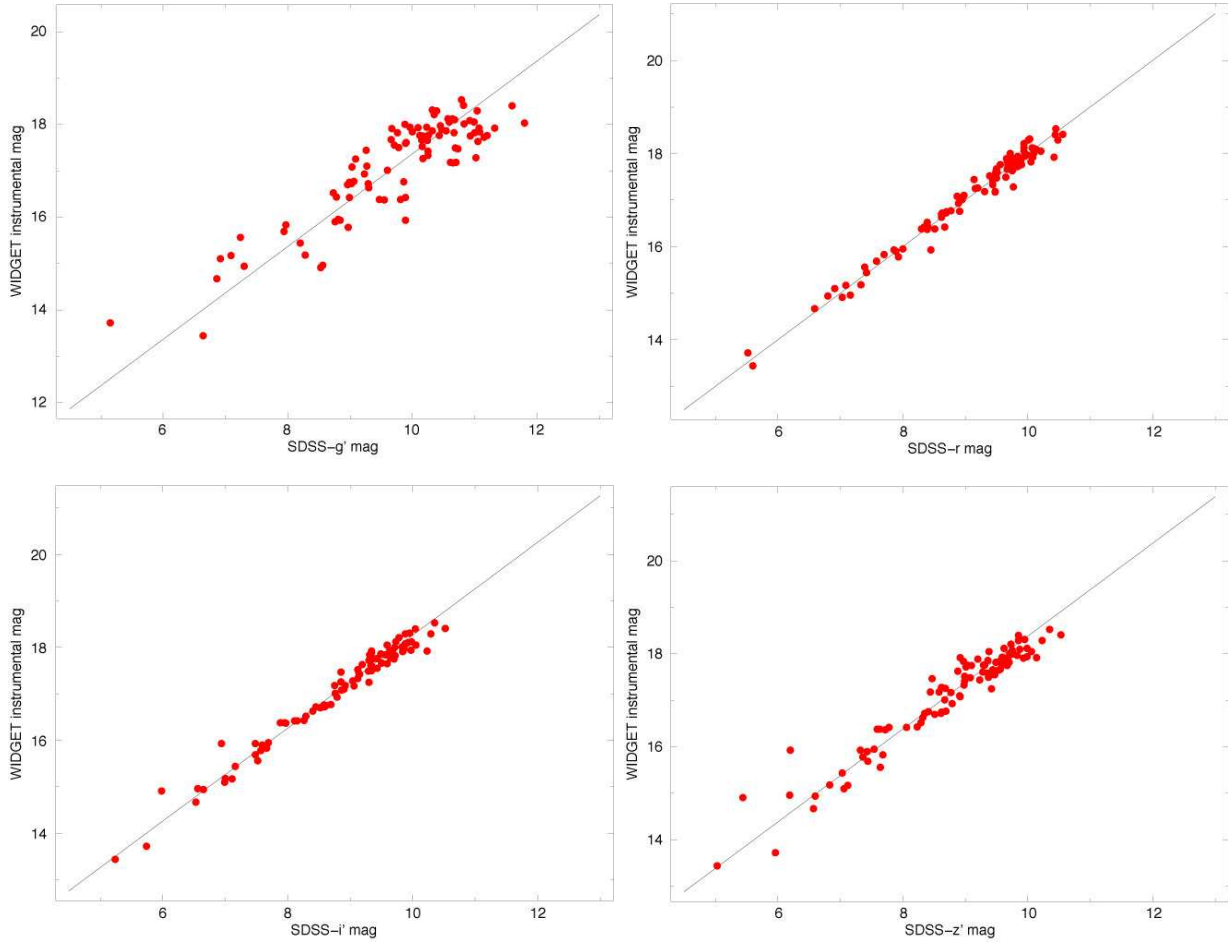


**Fig. 8.** The photometric calibration against with the Tycho-2.0 catalog translated to the SDSS  $g'$ ,  $r'$ ,  $i'$  and  $z'$  band system.

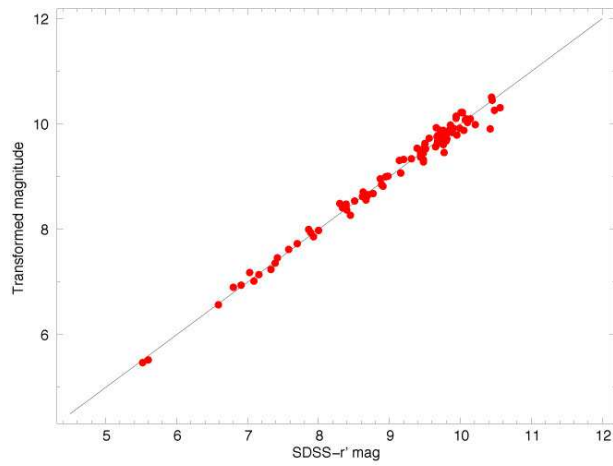


**Fig. 9.** The photometric calibration against with the Tycho-2.0 catalog translated to the SDSS  $r'$  band system.



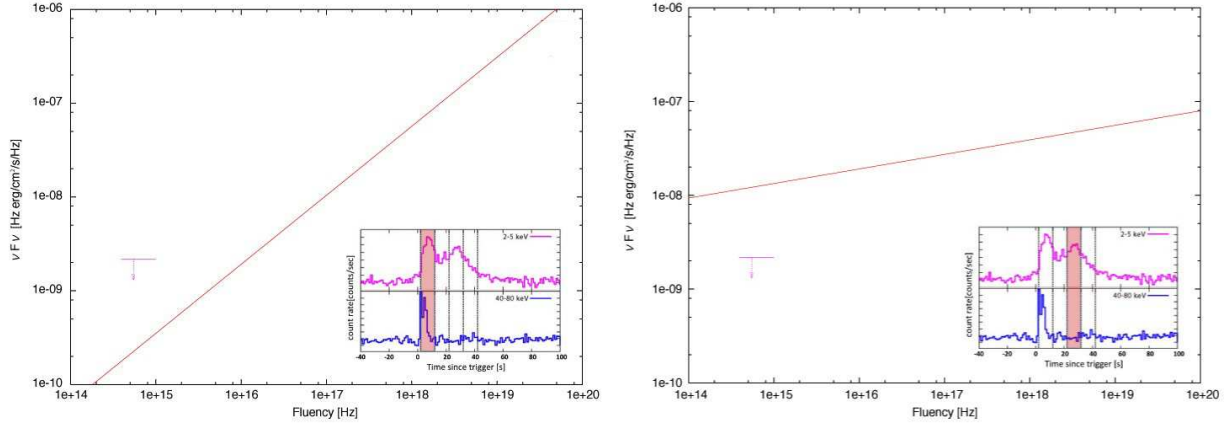


**Fig. 10.** Time resolved broad band SED of the GRB050408 prompt emission. Sub panels show the  $\gamma$ -ray and X-ray light curves. The red regions indicate the time region which we derive the SED. The lines show the best fit function of the low energy power-law.

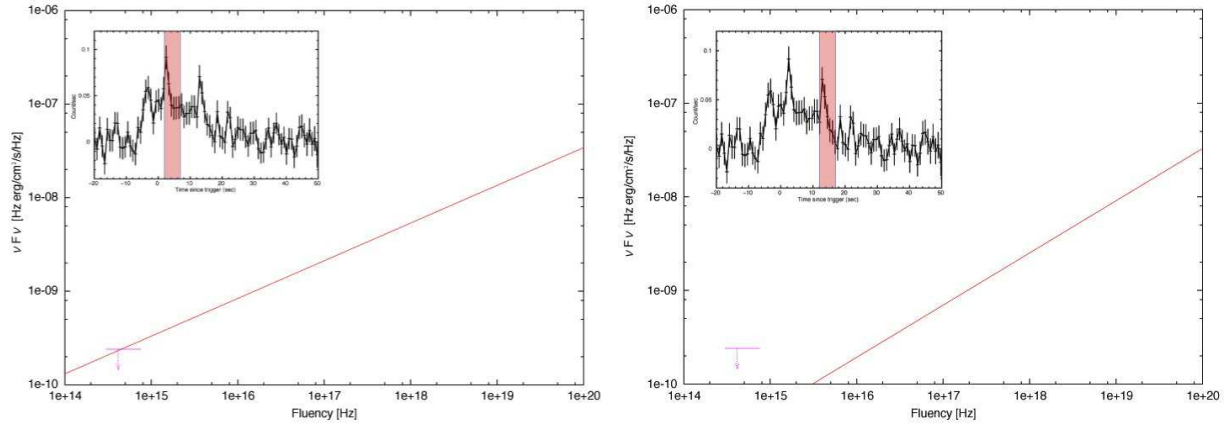


**Fig. 11.** Time resolved broad band SED for the GRB060323 prompt emission. Sub panels show the  $\gamma$ -ray and X-ray light curves. The red regions indicate the time region which we derive the SED. The lines show the best fit function of the low energy power-law.

**Table 2.** Comparison with other system

Name	Site	FOV	Limit	System	Ref
WIDGET	Kiso, Japan	$(32^\circ \times 32^\circ) \times 4$	12	CCD	This work
Pi of the sky	Las Capanas	$(20^\circ \times 20^\circ) \times 2$	$\sim 12.5$	CCD	Sokolowski et al. (2009)
TORTORA	La Silla	$30^\circ \times 24^\circ$	$10 \sim 11$	TV-CCD	Greco et al. (2009)
RAPTOR-Q	Fenton Hill, USA	All sky	9.5	CCD	Wozniak et al. (2009)
RAPTOR-P	Fenton Hill, USA	$(8^\circ \times 8^\circ) \times 4$	15	CCD	Wozniak et al. (2009)

**Table 3.** GRB Observation summary

GRB	Localization	Time coverage	$z$	T90 [s]	Fluence*	Earliest follow-ups	OT
050408	<i>HETE-2</i>	-6.0 h - +3.4 m	1.24	19.9	50.5 <sup>†</sup>	ROTSEIIIa (18.5s)	Lulin $R = 20.3$
051028	<i>HETE-2</i>	-16.0 m - +11.2 m	--	18.8	60 <sup>†</sup>	Lulin (2.28h)	$R = 20.8$
051227	<i>Swift</i>	-187 m - +12 m	0.71	114.6	7.0 <sup>‡</sup>	RIMOTS (20 min)	VLT $R \sim 25$ (10)
060121A	<i>HETE-2</i>	-8 h - -3.5 h	--	3.6	70.2 <sup>†</sup>	NOT (1.98h)	$R = 22.65$
060211A	<i>Swift</i>	-13.2 m - +5.4 m	--	126.3	15.7 <sup>‡</sup>	ROTSEIIIa (147s)	$R < 14.3$
060323	<i>Swift</i>	-12.5 m - +1.4 m	--	25.4	6.2 <sup>‡</sup>	Xinglong (540s)	$R = 18.2$
060413	<i>Swift</i>	-0.4 m - +5.6 m	--	147.7	35.6 <sup>‡</sup>	UVOT (124s)	$V < 19.2$
070616	<i>Swift</i>	-0.5 m - +2.7 m	--	402.4	192.0 <sup>‡</sup>	MITSUME (23m)	BTA $R \sim 22$ (7)
070810B	<i>Swift</i>	-1.2 m - 20.1 m	--	0.08	0.12 <sup>‡</sup>	Xinglong (300s)	$R < 20.5$
071021	<i>Swift</i>	-13.4 m - +140.8 m	--	225	13 <sup>‡</sup>	Faulkes (258s)	$R = 17.8$
090408	<i>Swift</i>	-20.0 m - +3.0 m	--	--	--	TAOS (91s)	$R < 15.2$

\*:  $10^{-7}$  erg cm<sup>-2</sup>

†: 30-400 keV band

‡: 15-150 keV band